Features of the modelled stress-strain state dynamics prior to the M 7.1 2019 Ridgecrest earthquake in Southern California

Valery G. Bondur[1], Mikhail B. Gokhberg[1,2], Igor A. Garagash[1,2], and Dmitry A. Alekseev[1,2]

The paper is concerned with the analysis of the simulated stress-strain state (SS) parameters of the Earth's crust over the four-year period preceding the M7.1 2019 Ridgecrest earthquake in Southern California. SS parameters have been calculated using a detailed geomechanical model, taking into account an ongoing weak seismicity catalog data. Cyclic patterns are identified in the observed shear strain anomalies, with estimation of their spatial and temporal characteristics, and an attempt is made to track the influence of the local displacement direction and periodic migration of shear strain anomalies in the upper crust on the earthquake preparation. Finally, we discuss the role of the observed regularities in terms of existing models describing the earthquake preparation process. *KEYWORDS:* Geomechanical modelling; shear strain; earthquakes; stress-strain state; stress anomaly excursions; precursors, monitoring; South California; Ridgecrest.

Citation: Bondur, Valery G., Mikhail B. Gokhberg, Igor A. Garagash, and Dmitry A. Alekseev (2022), Features of the modelled stress-strain state dynamics prior to the M 7.1 2019 Ridgecrest earthquake in Southern California, *Russ. J. Earth. Sci., 22,* ES5002, doi:10.2205/2022ES000798.

1. Introduction

A series of Ridgecrest earthquakes, with magnitudes ranging from 5.4 to 7.1, occurred in Southern California during 4–6 July 2019, with the main M7.1 shock of 6 July being one of the largest seismic events in this region in recent years. Given the dense population and the existing risk of strong and catastrophic earthquakes, the problem of seismic monitoring in Southern California has received noticeable attention [*Clayton et al., 2015*; *Hutton et al., 2010*]. At the same time, despite the huge amounts of seismological and geodetic data being collected in the region, the precursory patterns identification and short-term forecast still remains far from success.

The issues of short-term earthquake forecast have been widely researched for decades using various approaches, including the background seismicity analysis [*Mogi, 1985*; *Molchan and Keilis-Borok, 2008*], search and detection of various geophysical precursors [*Sobolev and Ponomarev, 2003*], and satellite-based monitoring techniques [*Akopian et al., 2017*; *Bondur and Zverev, 2005*; *Bondur et al., 2007, 2018*]. An important contribution is made with implementation of high-detail geomechanical models [*Bondur et al., 2016*], taking into account the current state of the crust in the studied region. This approach allows overcoming the problem of weak manifestation of deep stress accumulation and deformation processes on the Earth's surface, which complicates their detection by means of direct monitoring techniques [*Bondur et al., 2020a*]. Another line of research is focused on the study of the mechanical stability of seismically active crustal zones, where the seismic process is con-

---

[1]Institute for Scientific Research of Aerospace Monitoring "AEROCOSMOS", Moscow, Russia

[2]Schmidt Institute of Physics of the Earth RAS, Moscow, Russia

sidered to be confined within the already existing faults, and coseismic motions develop under conditions of limited mobility of the fault-separated blocks. Typical behavior of such geomechanical systems can be described, for example, assuming avalanche unstable fracturing model [*Sobolev,* 2019] or the dilatancy-diffusion concept (DD) [*Main et al.,* 2012; *Myachkin et al.,* 1975]. In those models the process is reduced to the destruction of the so-called bridge between two cracks and is reproduced in laboratory experiments on rock samples [*Sobolev,* 1993]. The available shear stress monitoring data suggest that the formation of a dumbbell-shaped, elongated region with positive principal shear stresses having two local maxima of no more than 20–30 km apart might be considered as indication of the earthquake preparation [*Garagash,* 2000].

To study the stress-strain state dynamics in connection with strong earthquakes in Southern California (Figure 1), since 2009 we have been performing simulation-based geomechanical monitoring employing a 3-D detailed SS model that takes into account ongoing seismicity data from USGS catalog. The model is iteratively updated in a way that every single earthquake with magnitude over 2 is considered as a new defect in the Earth's crust, having appropriate dimensions and degree of destruction, and leading to the stress state redistribution. By calculating various SS parameters, the model allows simulating the destruction and healing of the Earth's crust; identifying elastic energy accumulation and relaxation patterns; revealing migration paths of anomalous stress and deformation zones, and tracking changes in the displacement field at different depths within the Earth's crust prior to strong seismic events ($M > 7$) occurring in this area [*Bondur et al.,* 2010, 2016, 2020b].

In this study, on the base of the above geomechanical model and seismicity magnitude timeseries for the period from 1 January 2016 to July 2019, we analyze crustal stress-strain state variations in Southern California within the area of the 2019 Ridgecrest earthquake, limited within 35–36°N latitude and 116.4–118.6°W longitude. Main task of the analysis is concerned with identification of cyclic patterns in the shear strain anomalies observed from simulated data, evaluation of their spatial and temporal characteristics, and attempt to detect the connection of the modelled incremental

displacement orientation in the upper crust with the preparation of the Ridgecrest earthquake. Below we provide detailed explanation of the modeling procedure and relevant parameters.

2. Methods

The analysis provided in this study is made on the grounds of a geomechanical simulation-based monitoring technique described and discussed in [*Bondur et al.,* 2016, 2020b]. The model allowed monitoring the stress-strain state dynamics for the region in question based on local current seismicity data during time interval from 2009 to 2019. Modeling domain covers the area between 31 and 36°N latitude and 114 and 121.2°W longitude, and has a 6-layer structure within 0–35 km depth interval. Layer boundaries are specified according to available data, including topography/bathymetry, sediment thickness, upper/lower crust and Moho surface [*Bondur et al.,* 2016]. The geometry data for main structural elements have been taken from [*Parsons,* 2006]. The domain is discretized by rectangular prism mesh with lateral spacing of 5×5 km, where each element is assigned the specific set of material properties K, G, c and φ, which denote the bulk modulus, shear modulus, cohesion and angle of internal friction, respectively (Table 1).

Given that the area is characterized by a complex fault tectonics [*Wallace,* 1990], to represent the destructed portions of the crust, we apply the so-called crustal damage function $g(x, y, z)$ to correct the prespecified values of material property in any given layer (for specific z):

$$P(x, y) = P_0(1 - \kappa g(x, y)).$$

Here P is either elastic modulus or cohesion or friction, P_0 – its initial value, corresponding to the intact structure, and $\kappa < 1$. Function $g(x, y)$ has the meaning of the normalized spatial distribution of dimensionless parameter taking values between 0 and 1, produced from fault maps, surface topography/bathymetry and satellite imagery data [*Bondur et al.,* 2016]. To calculate $g(x, y, z = 0)$, the fault map was projected onto the model grid, and maximum crustal destruction $g = 1$, was set for the meshes crossed by the fault lines. On the other hand, the condition $g = 0$ was used for the meshes far enough (3-fold of the lateral mesh size)
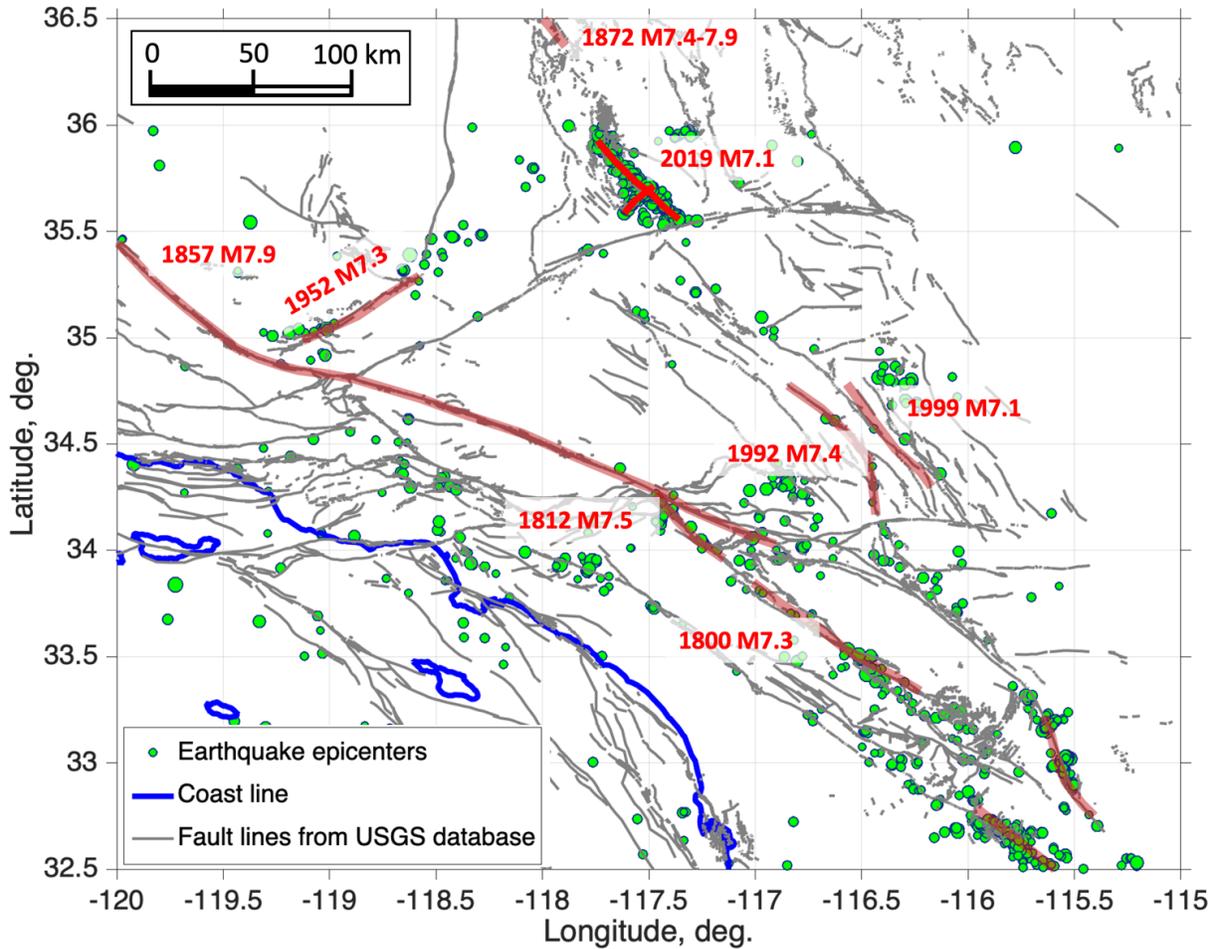
Figure 1. Fault map (gray lines, USGS database) and seismicity ($M > 1$, green circles, ComCat catalog) in Southern California region. Light brown lines show the surface ruptures associated with the largest earthquakes ($M > 7$) according to historical data. The faults related to the $M6.4$ foreshock and $M7.1$ main shock of 2019 Ridgecrest earthquake are shown in bright red.

Table 1. Averaged Values of the Mohr-Coulomb Model Parameters Originally Assumed for 6 Laterally-Homogenous Model Layers at the Initial Stage of Model Construction, Followed by Application of "Damage Function" to Produce Heterogenous Property Patterns (See Figure 2)

Model layer (element)	Bulk modulus, GPa	Shear modulus, GPa	Angle of internal friction, °	Cohesion, MPa	Density, kg/m^3
L1 Upper crust	17.3	8	26	20	2600
L2 Upper crust	19.5	9	30	35	2700
L3 Middle crust	16.2	7.5	27	32	2700
L4 Middle crust	14.5	6.7	25	29	2800
L5 Middle crust	11.9	5.5	24	26	2800
L6 Lower crust	18.4	8.5	27	30	2800

from the nearest fault. Then the 2-D smoothing spline was applied to produce the smooth distribution of $g(x, y)$ at the Earth's surface, i.e., for the upper layer L1. For every layer lying deeper, the damage distribution was calculated from the shallower one by spatial smoothing, with smoothing window size increasing with depth, thus producing a full 3-D mesh-projected grid $g(x, y, z)$. Resulting model properties distributions are shown in Figure 2.

To calculate the stress-strain state evolution, we assume Mohr-Coulomb constitutive model and utilize FLAC3D software code [*Itasca...*, 2006], solving the continuum mechanics equations with explicit finite-difference method in a series of simulations as following. At zeroth step, the model is subjected to gravity and regional-scale tectonic-related forces, with latter being applied in the form of the GPS-measured motions, taken from the NUVEL-1 model [*Argus and Gordon,* 1991]. Assuming the static approximation, this results in initial (stationary) state of the model, $SS(x, y, z, t_0)$.

Initial calculation is followed by an iterative loop, where the stress-strain state is updated based on sequential corrections to geomechanical parameters (bulk and shear moduli, cohesion and friction angle), which is applied to mesh elements that had been affected by seismic events during a 3-month time interval prior to the time of the calculation t_i:

$$SS(x, y, z, t_0) \to \ldots \to SS(x, y, z, t_i) \to$$

$$SS(x, y, z, t_{(i+1)}).$$

Current local seismicity data in the form of foci locations and magnitudes ($M > 1$) are extracted from USGS ComCat catalog (U.S. Geological Survey, ANSS Comprehensive Earthquake Catalog, https://earthquake.usgs.gov/data/comcat/), and projected onto the model grid, with calculation of the released energy values E from magnitudes M:

$$\lg E = 4 + 1.8M.$$

The total energy release in each cell over 3-month period (with about 4 thousand individual shocks occurring on average within modelling area) is estimated by summation of individual magnitudes.

It should be noticed that in doing so, the foci positioning errors and grid interpolation bias reduce due to averaging of significant amount of events, and the resulting accuracy of the model in terms of lateral distance is estimated as 1–2 x mesh size. Smoothed distributions $E(x, y, z, t_i)$ and the previous-step SS are applied to calculate the updated damage function:

$$g(x, y, z, t_{(i+1)}) =$$

$$f_{DM}(E(x, y, z, t_{(i+1)}), SS(x, y, z, t_i)).$$

Here f_{DM} transforms the current-step energy distribution E into updated damage distribution g_{i+1} = $g(x, y, z, t_{i+1})$. This transform involves calculation of maximum shear stress

$$\tau_{\max}(x, y, z, t_i) =$$

$$\sqrt{\frac{1}{6}[(\sigma_{xx} - \sigma_{yy})^2 + (\sigma_{yy} - \sigma_{zz})^2 + (\sigma_{zz} - \sigma_{xx})^2] +}$$

$$\overline{\sigma_{xy}^2 + \sigma_{yz}^2 + \sigma_{zx}^2},$$

and shear energy

$$E_S(x, y, z, t_i) = \frac{\tau_{\max}^2}{G},$$

from which, and updated damage function g is evaluated:

$$g(x, y, z, t_{i+1}) =$$

$$\frac{E(x, y, z, t_{i+1})}{E(x, y, z, t_{i+1}) + E_S(x, y, z, t_i)}. \tag{1}$$

In turn, g is applied to update the model parameters:

$$P(x, y, z, t_{i+1}) =$$

$$f_{MD}(P(x, y, z, t_i), g(x, y, z, t_{i+1})).$$

Specifically,

$$P_{i+1} = (P_i - \Delta P_i \cdot r) \cdot (1 - \kappa g_{i+1}).$$

Here P is either bulk modulus K, shear modulus G, cohesion or angle of friction φ, $\Delta P_i = P_i - P_{i-1}$ indicates the damage-associated increment added to the previous-step property value, while $r = 1/8$ is the recovery factor applied to account for "rock healing" by 1/8 every two weeks (which means if no new earthquakes occur within a particular mesh element, its properties' values return back to original values within 4 months), $\kappa = 0.3$ is a small
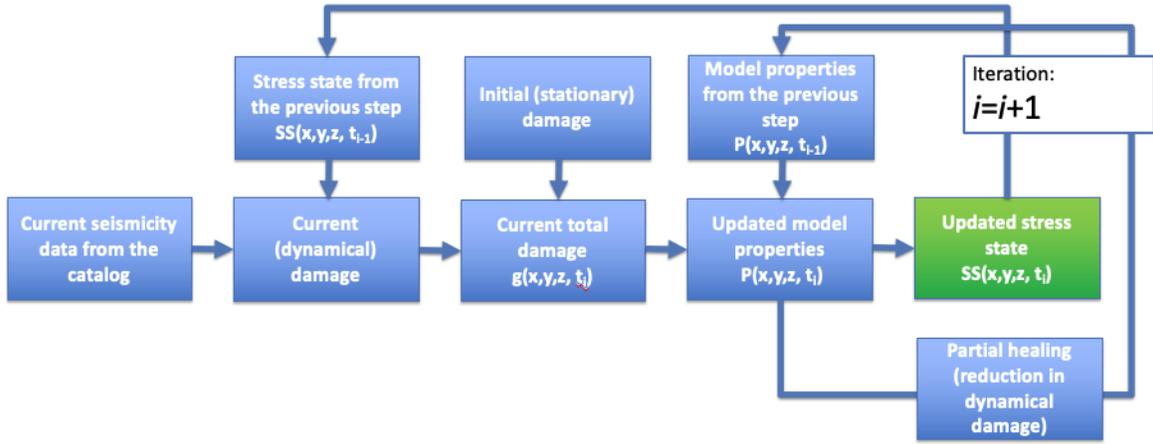
Figure 3. Schematic representation of the stress-strain state simulation cycle.

term and $g_{i+1} = g(x, y, z, t_{i+1})$ is normalized damage function defined by (1).

Once the corrected model P is obtained, it is used to run geomechanical simulation and compute an updated stress-state distribution:

$$SS(x, y, z, t_{i+1}) = f_{SS}(P(x, y, z, t_{i+1})).$$

Unlike the explicit algebraic functions f_{DM} and f_{MD}, the transform f_{SS} denotes a procedure of solving geomechanical problem (equation of motion) in static approximation using FLAC^{3D} finite-difference code yielding the complete set of both stress and strain tensor elements.

Thus, the sequential evaluation of f_{DM}, f_{MD}, and f_{SS} transforms repeated with time step

$$\Delta t = t_{i+1} - t_i = 1/2 \text{ months,}$$

provides series of strain-state parameters. General scheme of simulation procedure is given in Figure 3.

The computed SS datasets are used to calculate and visualize the most important kinematic quantities, displacement increment $u = \{u_x, u_y, u_z\}$, and shear strain intensity (shear deformation, SD) γ:

$$\gamma =$$

$$\sqrt{\frac{1}{6}[(\varepsilon_{xx} - \varepsilon_{yy})^2 + (\varepsilon_{yy} - \varepsilon_{zz})^2 + (\varepsilon_{zz} - \varepsilon_{xx})^2] +}$$

$$\overline{\varepsilon_{xy}^2 + \varepsilon_{yz}^2 + \varepsilon_{zx}^2},$$

where ε_{ij} are the strain tensor elements.

The distributions of the horizontal component of the displacement in any given model layer are presented in the form of arrows, scaled according to displacement magnitude. The shear strain intensity is displayed in the form of color maps.

Special attention is paid to the analysis of the directions between the horizontal incremental displacement vectors and averaged orientation of the rupture associated with Ridgecrest earthquake. Considering its southeastern direction (with approximate bearing of 125 degrees) as zero, and calculating the angles of deviation of the displacement vector from this (tangential) direction (Figure 4), we obtained a series of maps and revealed some specific patterns, which are discussed in the following section.

3. Results

Below we analyze and discuss peculiarities of the simulated kinematics for model layer 2 (L2, upper crust), accommodating most of seismicity in the area.

3.1. Stress-Strain State Dynamics During the Early Stages of Ridgecrest Earthquake Preparation

The $M7.1$ Ridgecrest earthquake occurred on July 6, 2019 in Southern California (epicenter lo-
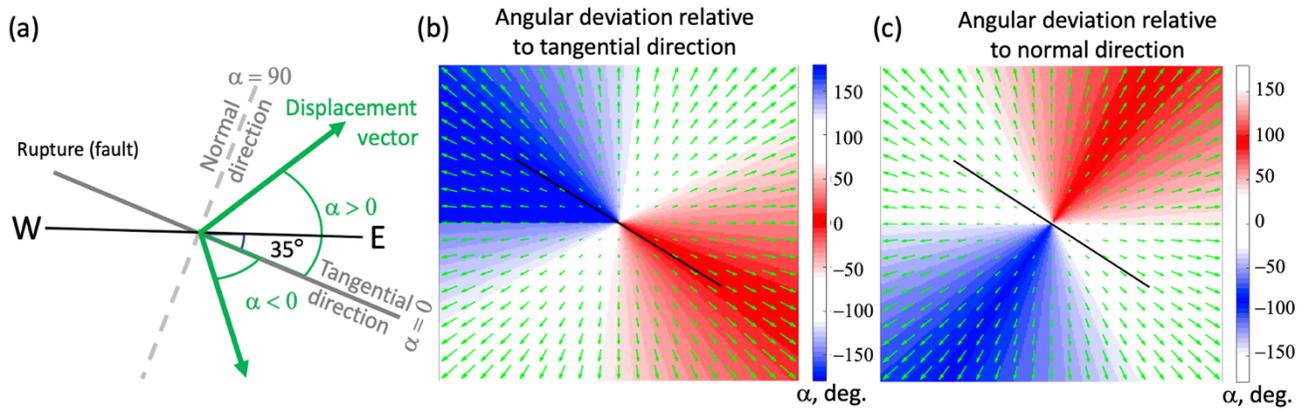
Figure 4. (a) Calculation of the angular deviation between the horizontal displacement and linearized Ridgecrest earthquake rupture; (b) Colormap of angular deviation of the displacement vectors (green arrows) from tangential direction relative to the earthquake rupture (black line, zero corresponds to South-Eastern direction; (c) Colormap of angular deviation of the displacement vectors (green arrows) from tangential direction relative to perpendicular to the earthquake rupture.

cation 35.766°N, 117.605°W) and falls next to the cluster of the so-called East California Shear Zone (ECSZ), where Hector Mine earthquake (1999) and Landers earthquake (1992) took place (Figure 1).

The stress-strain state dynamics analysis was based on space-time distributions of the shear strain intensity (SD) magnitudes and displacement vector according to the above-described technique. The main results are presented for the second layer (L2) of the upper crust (3–7 km depth range), accommodating most of the current seismicity in Southern California. In [*Bondur et al., 2021*], it is shown that signs of short-term precursors of this earthquake begin to appear as early as 3 years before the event. Starting from May 2016 and over the entire period of preparation, abrupt changes in the anomalous SD values are observed, with some periods of quiescence, only seen within the future epicentral zone (EZ) (Figure 5a). Such patterns of SD alternation, with peaks and gaps, are called "excursions" (by analogy with excursions of the Earth's magnetic pole). Excursions follow a specific behavior, where sharp increase in SD levels, significantly exceeding the background, does not lead to an earthquake, but rather gives way to its decrease, with stress state returning back to quiescence. This cycle may repeat several times until the earthquakes ultimately occurs. Figure 5a shows 5 distinct excursions identified during period from 2016 to July 2019. Formation of clam

periods (quiescence) might be explained in terms of the well-known avalanche unstable fracturing model [*Sobolev, 2019*] and the dilatancy-diffusion model (DD) [*Main et al., 2012*; *Myachkin et al., 1975*]. Possible mechanism behind this behavior involves pore pressure decrease during the opening of cracks, causing the rock hardening.

During a quiescence, when the rocks in the EZ do not experience substantial displacements, the external tectonic forces continue to act, which leads to a redistribution of the maximum SD to the nearest surrounding area until the rocks in the EZ return to an unstable state. This behavior resembles "swinging" and is demonstrated in Figure 5b. The swing period T is on the order of several months, and the SD changes, i.e., transitions between background and peak values, occur relatively quickly (0.5 months), and reach about 10^{-4}, according to modelled data. The swing distance R does not exceed 100–150 km, and the characteristic size of the largest SD anomalies, r is around 20 km.

At the same time, the presence of the so-called "excursions" and "swings" raises a number of questions. Indeed, the early manifestation of such processes indicates just the beginning of the earthquake preparation. However, analyzing those data alone, it is impossible to predict which particular excursion cycle will end up with a great earthquake. The latter can lead to the difficulties in application of these results for short-term forecast due to high
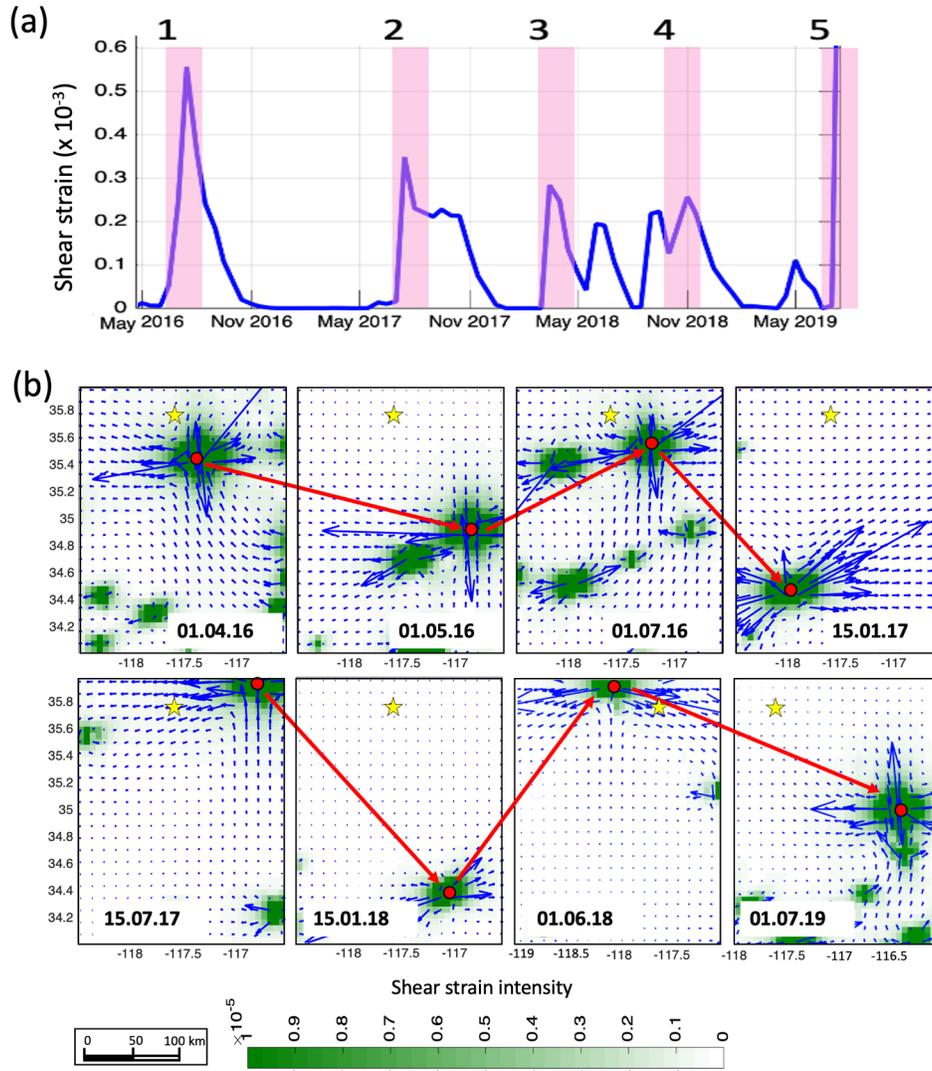
Figure 5. (a) Shear strain (SD) excursions in the epicentral zone (shown by pink bars and numbered as 1 to 5); (b) Migration cycles of the SD anomaly from within the epicentral zone to outer region and back.

chance of false alarms. Thus, both additional data and a detailed analysis with the possible involvement of some new parameters are needed. In the following sections, we focus on the attempt to limit the above-mentioned ambiguity.

3.2. Increase in Seismic Activity Associated With San Andreas Fault

Since the main shock of Ridgecrest earthquake had magnitude of 7.1, its source's length is estimated at about 60 km, and entire area of South-ern California covered by geomechanical model, should be considered as a region affected by the earthquake preparation process in the subsurface. Within the modelling domain, the San Andreas fault has a length of about 600 km. Figure 6a, Figure 6b show the spatial distributions of shear deformation intensity (SD) and incremental displacements as of Feb. 15, 2018 and Nov. 15, 2018, respectively.

The virtual absence of activity (Figure 6a), except for a local anomaly occupying a relatively small area in the NW part of the fault, is typical for the beginning of year 2018. Figure 6b shows
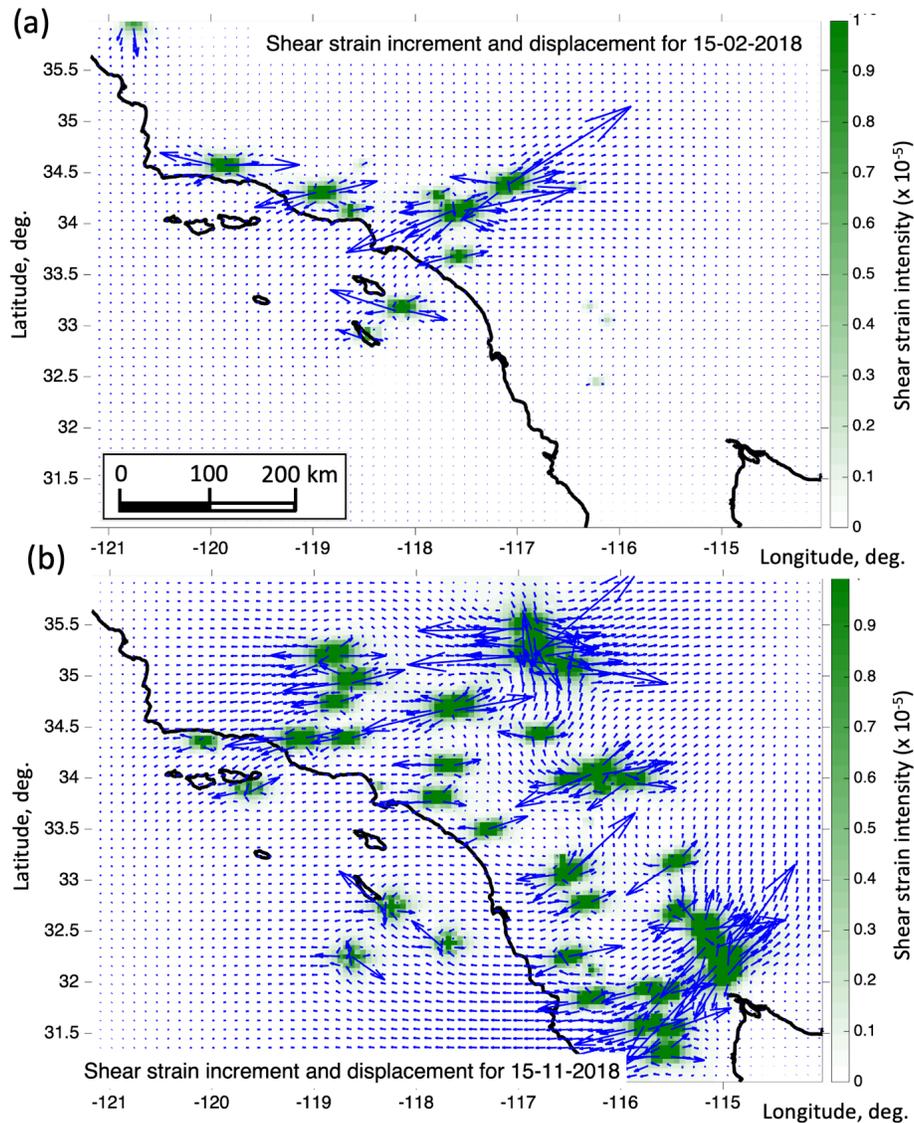
Figure 6. Distributions of shear strain intensity (green-colored imagemap) and incremental displacement vectors as of Feb. 15, 2018 (a) and Nov. 15, 2018 (b).

the most intense SD pattern, which has developed at the end of the year 2018 – beginning of the year 2019. A 100 km-wide zone accommodating most of SD anomalies follows the fault throughout its entire length, while the displacement vectors exhibit chaotic orientation.

Figure 7a indicates the variations of the fault-activation-intensity, an integrated approximate measure showing the level of seismic and geo-dynamical activity, calculated (for individual anomaly) as the product of maximum SD and anomaly size. As can be seen from this figure, the elevated levels of this parameter are observed about

half a year prior to the event, which is interpreted as the phase of maximum development of the large-scale earthquake preparation process.

3.3. Displacement Field Orientation Dynamics

Orientation of displacement vectors is an important parameter for monitoring the stress-strain state dynamics of the Earth's crust during the preparation of a large earthquake. This section provides a detailed analysis of the spatio-temporal
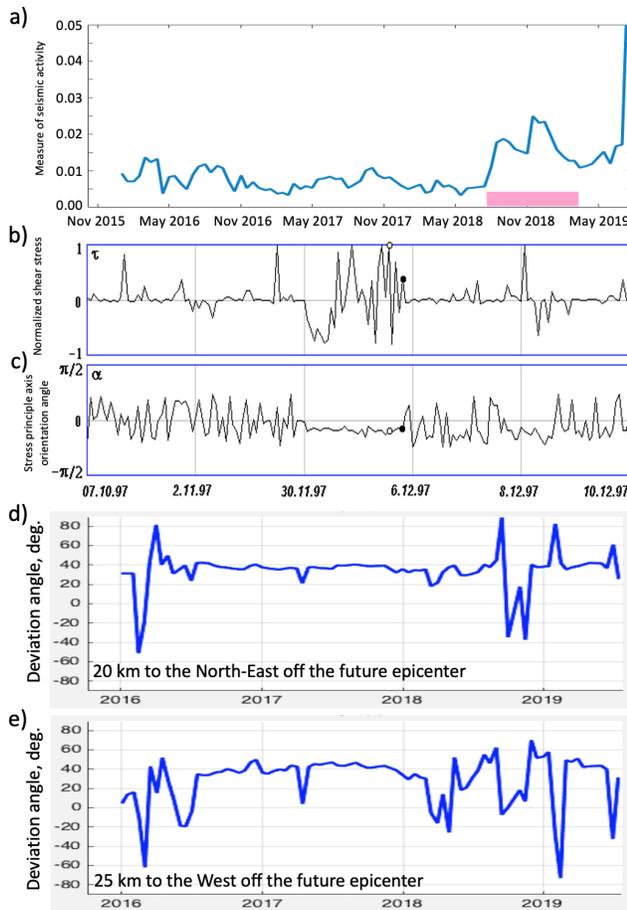
Figure 7. (a) Variations of the seismic activation intensity (nominal units) for Southern California area during the period of 2016–2019, estimated from shear strain distributions. (b) Normalized variations of principle stress and (c) stress tensor principle axis orientation in the vicinity of large earthquake of Dec. 5, 1997 in Kamchatka. The seismic event is shown by black point (modified from [*Garagash,* 2000]. Panels (d) and (e) show angular deviations of the incremental displacement vector from predominant orientation of the Ridgecrest earthquake rupture at two different locations from both sides of the rupture.

distribution of the horizontal displacement direction, calculated for the model layer 2 (3–7 km depth) during time interval from 2016 to 2019, preceding the $M7.1$ Ridgecrest earthquake of 6 July 2019.

Garagash [2000] introduced the concept of stabilization of the shear stress axes. In that study, concerned with the $M7.9$ Kronotsky earthquake that occurred on 5 December 1997 in Kamchatka, orientation of the principal axis was found to remain unchanged for a long time prior to the event, and

this direction was consistent with the rupture (Figure 7b, Figure 7c). Figure 7d, Figure 7e show similar graphs for the angular deviation of the displacement relative to the Ridgecrest earthquake main rupture at two locations within the epicentral zone. These plots show variability of the angular deviation over time, however, they do not give an idea of the space-time dynamics of displacement orientation across the modelling area. To better understand its behavior and recognize certain patterns, we calculated the angular deviation between the modelled incremental displacements and true direction of the rupture within the epicentral zone for the 2016–2019 period. The rupture geometry and coseismic shear displacements are clearly recognized from the satellite imagery data (Figure 8).

The resulting plots for the maximum values of the shear deformation are provided as a series of maps corresponding to the time instants of anomalous SD peaks in the excursions (see Figure 5a). Along the northeastern side of the rupture and in the adjacent area, the displacement vectors are directed from northwest to southeast (orange-red colored area in Figure 8), while they have opposite orientation along the southwestern side (blue colored region). We assume that similar displacement patterns simulated from the model prior to the event are preferable for creating the necessary shear deformation in the future source.

From the displacement field analysis, the tangential component (with respect to the rupture) which determines the shear process in the source region, can be identified, as well as the normal component. This decomposition can give an idea of the appearance of zones of compression and extension in the future source area. To discriminate the tangential component, we calculated angular deviation for the given displacement vectors distribution and rupture orientation as shown in Figure 4b. The deviations close to 0 (SE) and 180 (NW) degrees are red-colored and blue-colored, respectively. Similar colormap is applied for the normal component, corresponding to deviations close to either 90 (NE) or 270 (SW) degrees (Figure 4c). The analysis was carried out in chronological order for the series of time instants corresponding to the stress-state excursions identified from Figure 5a.

During the first quiet interval in the region surrounding the epicentral zone (EZ), the shear strain anomaly is located on the southeastern continua-
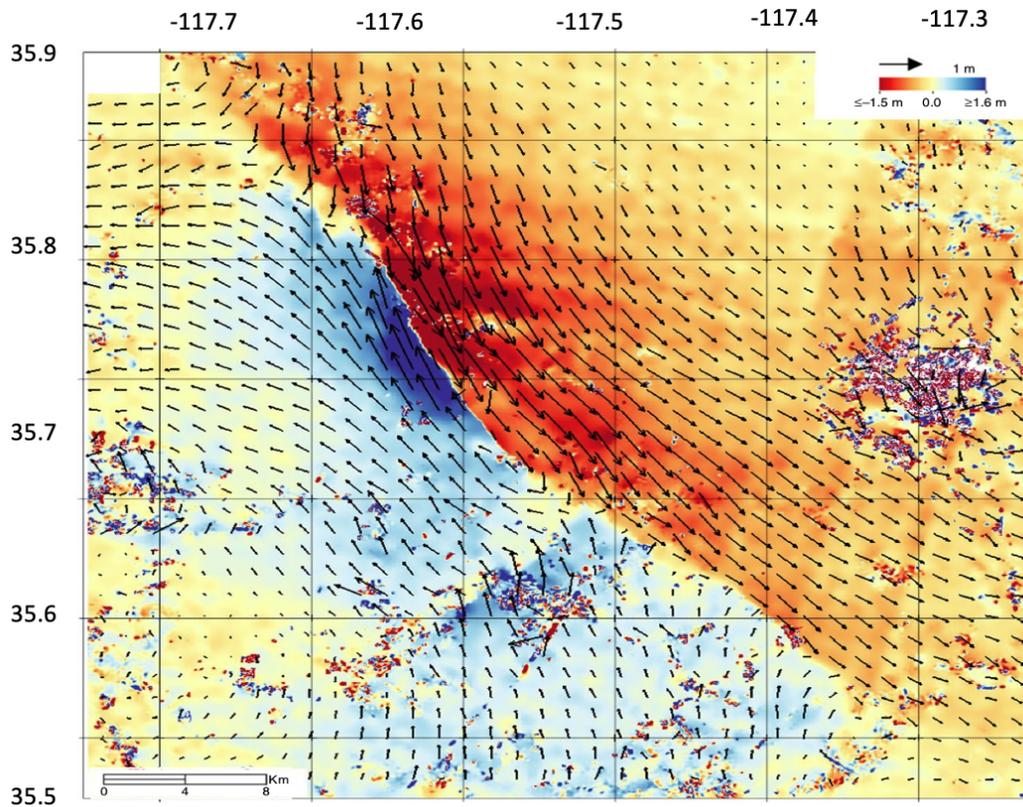
Figure 8. Surface displacements in the Ridgecrest area mapped by Sentinel-2 satellite imagery during Jun. 28–Jul. 08, 2019 (modified from [*Chen et al., 2020*]).

tion along the strike of the future rupture (Figure 9c), which creates the most favorable conditions in terms of displacement direction to be close to the tangential (Figure 9a), significantly prevailing over the normal component (Figure 9b). The directional pattern simulated for L2 model layer in May–June of 2016 practically coincides with the co-seismic surface displacements imaged satellite observations (Figure 8). For the tangential component, the sign change boundary (transition between red and blue) is slightly shifted to the south by the distance of about 10 km) in the SE part of the rupture.

However, this pattern does not persist during the SD peaks of excursion 1 (Figure 9, right panel). Despite the fact that the SD intensity is the highest for the entire time period of the earthquake preparation, the displacements' orientation is far from future faulting orientation (which is referred to as tangential) and, likely, because of this, the seismic event does not occur, and the stress-strain state (SS) returns to the quiescence. A similar situation is observed throughout excursion 2 until 15

March 2018 – the beginning of the SD increase in excursion 3. From this moment on, the elevated SD anomalies begin to appear immediately at the both ends of the future rupture in alternating manner, with the tangentially-directed displacements along the entire rupture length. Thus, the left panels of Figure 10 show angular decomposition (tangential-normal) maps (Figure 10a, Figure 10b), as well as the single shear strain anomaly at the SE end of the future rupture and displacement field modelled as 15 March 2018 (Figure 10c). Figure 10d, Figure 10e, Figure 10f and Figure 11a, Figure 11b, Figure 11c demonstrate similar settings, with the SD anomaly located at the rupture's northwestern and southeastern ends, respectively, i.e., as of 1 June 2018 (the pattern exists till 1 July 2018) and as of 15 November 2018 (the pattern is observed from August 2018 till February 2019).

At the same time, in Figure 10d, the boundary separating the regions of opposite orientation of the tangential component, is displaced along the entire length from the future rupture by the distance of about 30 km to the SW, while in Fig-
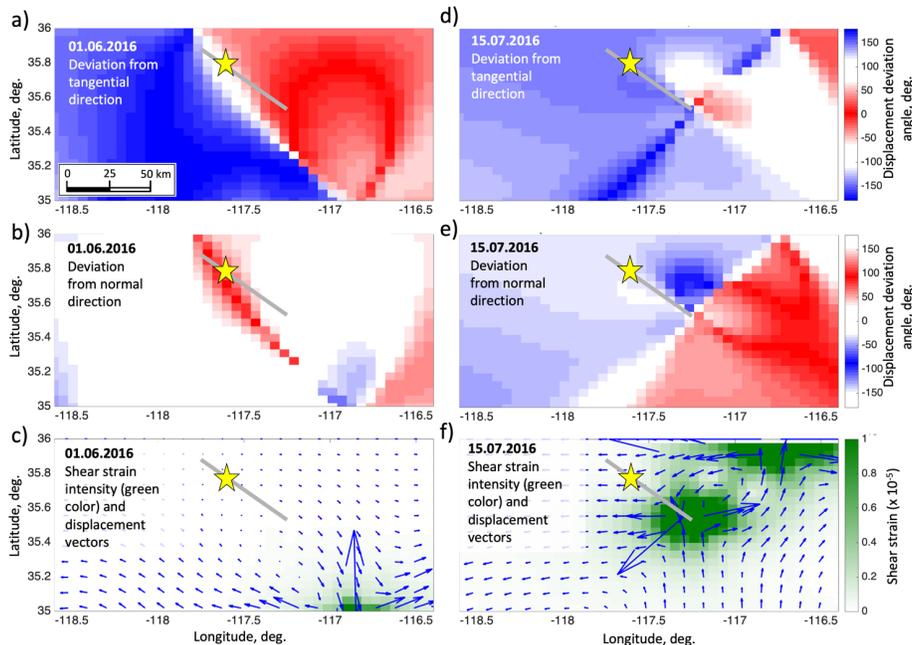
Figure 9. Ridgecrest rupture zone maps: Angular deviations of incremental displacement vectors from tangential direction (parallel to the rupture) during the quiet period before excursion 1 (01.06.2016) (a) and during the excursion (15.07.2016) (d); Angular deviations of incremental displacement vectors from normal direction (perpendicular to the rupture) as of 01.06.2016 (b) and 15.07.2016 (e); Shear strain intensity anomalies (green colormap) and incremental displacement vectors (blue arrows) as of 01.06.2016 (c) and 15.07.2016 (f).
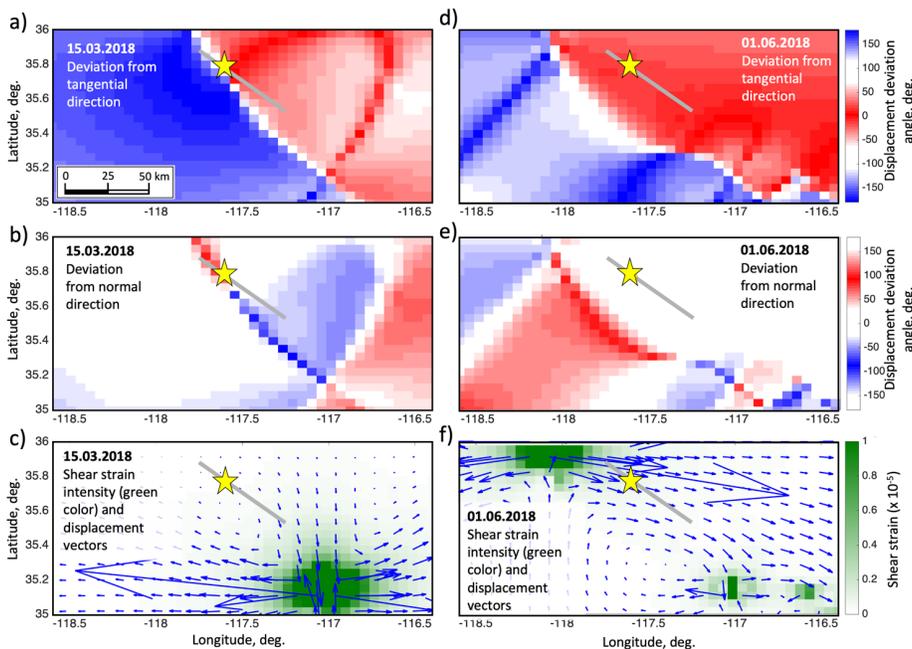

Figure 10. Ridgecrest rupture zone maps: Angular deviations of incremental displacement vectors from tangential direction (parallel to the rupture) as of 15.03.2018 (a) and 01.06.2018 (d); Angular deviations of incremental displacement vectors from normal direction (perpendicular to the rupture) as of 15.03.2018 (b) and 01.06.2018 (e); Shear strain intensity anomalies (green colormap) and incremental displacement vectors (blue arrows) as of 15.03.2018 (c) and 01.06.2018 (f).
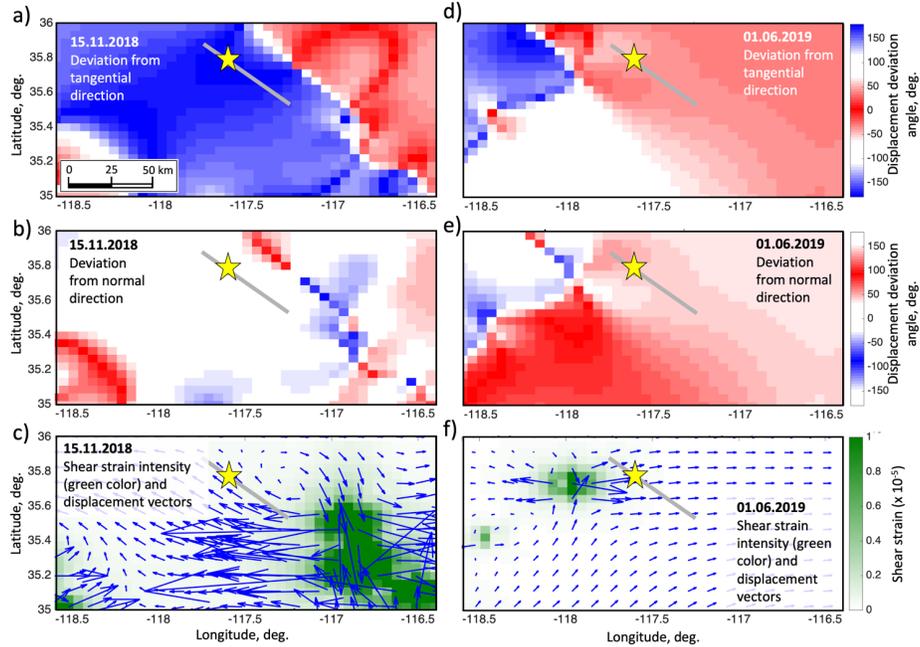
Figure 11. Ridgecrest rupture zone maps: Angular deviations of incremental displacement vectors from tangential direction (parallel to the rupture) as of 15.11.2018 (a) and during excursion 5, as of 01.06.2019 (d); Angular deviations of incremental displacement vectors from normal direction (perpendicular to the rupture) as of 15.11.2018 (b) and 01.06.2019 (e); Shear strain intensity anomalies (green colormap) and incremental displacement vectors (blue arrows) as of 15.11.2018 (c) and 01.06.2019 (f).

ure 11a such a displacement (by 20 km) is observed in the NE direction. Given that the spatial resolution of the model is determined by the mesh size (being 5×5 km), such distances are larger than resolution limits. The abovementioned boundary emerged as a result of calculation involving dozens of meshes accommodating hundreds of weak earthquakes with $M > 1$ according to the USGS catalog, and is sufficiently reliable. Thus, a relatively small difference between the locations of this boundary and a future rupture, which is observed until the last SD anomaly 5 days prior to the main shock, generally speaking, can somewhat affect the rupture preparation process.

Finally, 5 days prior to the earthquake, a redistribution of shear strain occurs, where the SD anomaly again falls at the southeastern continuation of the future rupture, while the displacements are close to tangential direction (Figure 12a). Besides, from the normal component distribution, an extension zone is recognized along the entire length of the future rupture (Figure 12b).

It should be noticed that the emergence of such a local extensional region 5 days before the Ridgecrest main shock provides additional favorable conditions for a shear (strike-slip focal mechanism).

The location of the last SD anomaly preceding the event nearly coincides with the shear zone of the $M7.1$ Hector Mine earthquake of 1999.

All of this evidence suggests that this shear strain anomaly was the final trigger responsible for the main shock preparation, with the overall stress-strain settings being most favorable for the energy release causing Ridgecrest earthquake. The above analysis shows the significant role of the simulated displacement orientation as an indicator of the seismic source preparation.

3.4. Source Formation and Bridge Destruction

In theoretical models, the rupture formation is considered as the destruction of the so-called "bridge" between two semi-infinite cracks [*Myachkin et al., 1975*], Figure 13a, or between the strain anomalies emerging before the sample rupturing simulated under laboratory conditions [*Sobolev, 1993*], Figure 13b.

Analysis of the spatial and temporal patterns of shear strain intensity and displacement directions prior to the Ridgecrest earthquake reveals that

Table 2. Parameters of the Swing Cycles Observed in Simulated SS Patterns in 2018 and 2019

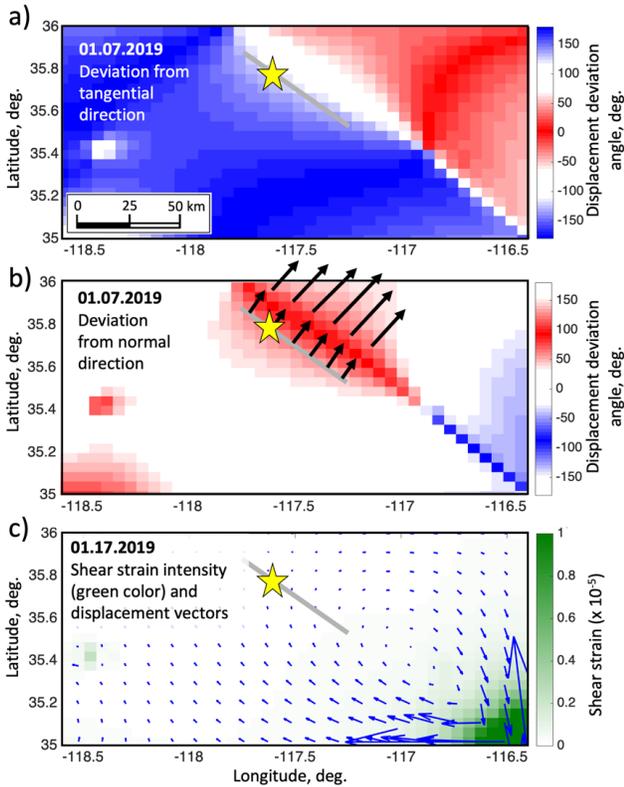| Cycle No. and anomaly location relative to the rupture	Date intervals when anomaly exists	Maximum SD intensity	Duration	Swing cycle period	Swing distance
1, SE	15.03.18–15.05.18	from 1×10^{-4} to 3×10^{-4}	2 months		
2, NW	01.06.18–15.07.18	$\sim 2 \times 10^{-4}$	1.5 months	0.5 months	~ 130 km
3, SE	01.08.18–15.02.19	from 1.5×10^{-4} to 2.5×10^{-4}	6.5 months	0.5 months	~ 130 km
4, NW	15.04.19–01.06.19	$\sim 1 \times 10^{-4}$	1.5 months	2 months	~ 100 km
5, SE	01.07.19	$\sim 3 \times 10^{-4}$		1 months	~ 160 km

Figure 12. Ridgecrest rupture zone maps as of 01.07.2019, 5 days prior to the Ridgecrest main shock: Angular deviations of incremental displacement vectors from tangential direction (parallel to the rupture) (a); Angular deviations of incremental displacement vectors from normal direction (perpendicular to the rupture) (e); Shear strain intensity anomalies (green colormap) and incremental displacement vectors (blue arrows) (f).

signs of a similar "bridge" destruction begin to develop about a year before the event. The dumbbell-shaped SD anomaly in the immediate vicinity of the NW and SE ends of the future rupture begins to appear starting from 15 March, 2018. Figure 14a shows two combined SD anomalies and displacement vectors, each in its location, calculated for 15 March and 1 June of 2018. The maximum of the SD intensity is first observed at the SE end of the future rupture, and then moves to the NW end. Redistribution in the opposite direction, from NW to SE is demonstrated in Figure 14b for two instants, 15 June and 1 September. Thus, a full cycle of SD anomaly alternation between the both sides of the "bridge" occurred, resembling the "swing".

It is interesting to note that when the second significant SD anomaly emerges in the west on Jan. 1, 2019, the original displacement field anomaly near the SE end acquires a vortex structure (Figure 14c).

Estimates of the swing cycle quantitative characteristics are presented in the Table 2, which contains data on 5 SD anomalies that occur alternately at the northwest and southeast ends of the "bridge".

Thus, the formation of the Ridgecrest earthquake focus, based on the above analysis, probably begins about a year before the event and manifests itself in the successive appearance of SD anomalies at the ends of the "bridge", which can be considered the first signs of its destruction.
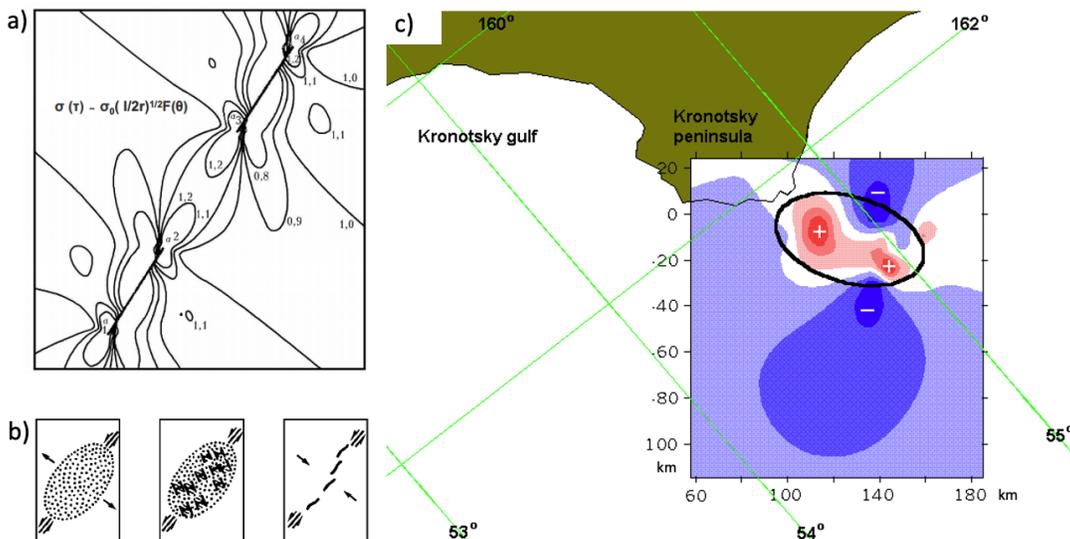
Figure 13. (a) Contourmap of maximum tangential stress calculated for a two-fracture model by [*Myachkin et al.*, 1975]; (b) Rupture formation staging according to the avalanche unstable fracturing model [*Sobolev*, 1993]. (c) Normalized maximum tangential stresses as of December 5, 1997 in Kronotsky bay area, 2 h 52 min prior to $M7.9$ earthquake (modified from [*Garagash*, 2000]). Black ellipse indicates the stress-concentration region corresponding to the rupture zone.
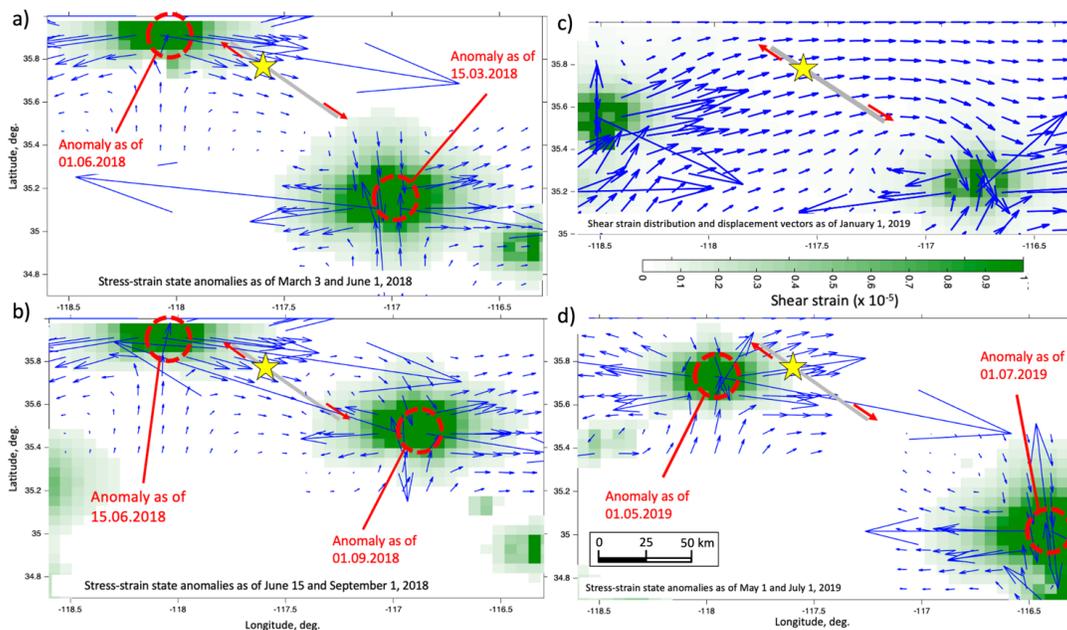

Figure 14. Combination of SD anomalies (image map) and displacement vectors (blue arrows), each in its location, identified at the southeastern and northwestern continuations of the future Ridgecrest rupture in March–June (a) and June–September (b) of 2018. Red arrows indicate the shear direction in the Ridgecrest fault. (c) Shear strain intensity and displacement vectors as of Jan. 1, 2019; (d) Combination of the stress-strain state, each in its location, identified at the southeastern and northwestern continuations of the future Ridgecrest rupture as of 1 May and 1 July 2019.

3.5. *M*6.5 Foreshock of 4 July 2019

The *M*6.5 foreshock occurred on 4 July 2019 southeast of the main shock. Figure 15a shows the corresponding rupture locations and focal mechanisms according to data by [*Chen et al.,* 2020]. The foreshock rupture had a direction nearly perpendicular to the main shock rupture, while both events had similar focal mechanisms. Despite the fact that the foreshock had a significantly lower magnitude, the simulated stress-strain dynamics contains some pattern consistent with the foreshock rupture preparation. Identification of that became possible with separate analysis of the tangential and normal (with respect to the main shock rupture) displacements.

During the final stages of the Ridgecrest earthquake preparation, the normal component is much weaker than the tangential component, which determines the shear process in the direction of the main rupture. At the same time, the normal component is associated with the preparation of the perpendicular rupture.

The distribution of the displacement orientation relative to the normal direction as of 01.04.2018, which remains the same for the interval from 15 March to 1 May 2018, is shown in Figure 15b. Figure 15c shows similar pattern as of May 15, 2018.

The intensity of the red color corresponds to the proximity to the direction of the normal component (from SW to NE), while the blue colors indicate the opposite direction. The boundary perpendicular to the direction of the main rupture corresponds to the right strike-slip and coincides with the future foreshock rupture. Thus, a weak ongoing seismicity, reflecting the process of crustal destruction prior to the major event, serving as an input to the geomechanical model, makes it possible to identify effects of the second order associated with the weaker event preparation (the foreshock). This result turned out to be possible only with the decomposition of the simulated displacement datasets into two mutually perpendicular components.

4. Discussion

According to recent review by *Kato and Ben-Zion* [2021], there are three main concepts used to explain the large earthquake preparation process,

the cascade-up, pre-slip and progressive localization. Cascade-up model assumes that the large earthquake preparation is associated with the progressive rock weakening caused by low-magnitude seismicity over prolonged time interval within the system of pre-existing faults, subjected to background tectonic stresses [*Yoon et al.,* 2019]. Pre-slip model has main focus on slow aseismic motion occurring in a particular fault prior to a large seismic event [*Dieterich,* 1992], and progressive localization concept deals with distributed stress and strain patterns evolving in a way such that shear deformation anomaly arises before a large-magnitude rupture [*Ben-Zion and Zaliapin,* 2020], essentially in no association with pre-existing faults.

The approach employed in our study partly involves concepts of both cascade-up and progressive localization frameworks, where background stress and strain field governed by regional tectonic forces and pre-existing faulting distribution is complemented with local weakening-healing caused by ongoing seismicity-associated rock damaging, which enables simulation of evolving stress and strain patterns over entire Southern California region. Background seismicity reflecting continuous destruction of the Earth's crust caused by tectonic forces, is mainly associated with San Andreas, Garlock and Mount faults. However, since the model incorporates catalogue-based low-magnitude seismicity data, converted into reduced strength to simulate generated rock damage, and actual (scattered) seismicity isn't confined to specific faults (although those play important role in stationary stress distribution), the computation of distributed stresses' and deformation's evolution through iteratively updating geomechanical properties (elastic moduli, etc.), delivers the SS variation across a fairly broad area around the future rupture.

The analyses within progressive localization model for Southern California given in [*Ben-Zion and Zaliapin,* 2019, 2020; *Kato and Ben-Zion,* 2021] indicate the evidence of progressive rock damage around the eventual rupture zones prior to the major ($M > 7$) events occurred in this region over the past decades, with clear localization during the final 2–3 years prior to the mainshocks. Above studies mainly focus on direct transform of observed seismicity into rock damage volume and localization, applying geostatistical estimates [*Molchan and Keilis-Borok,* 2008], with no use of
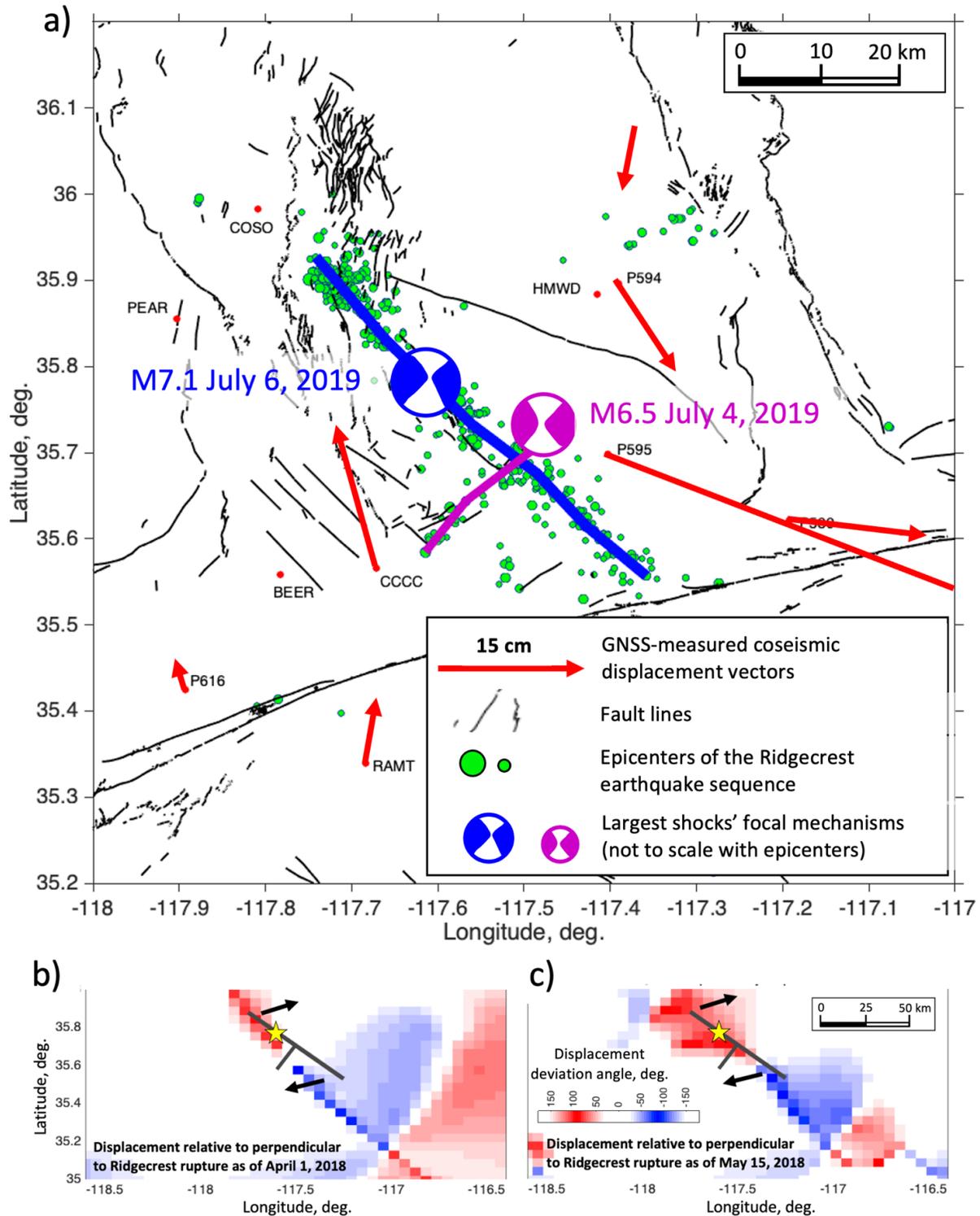
Figure 15. (a) Focal mechanisms of the largest Ridgecrest shocks and coseismic displacements according to measured GNSS data (red arrows). Blue and purple lines indicate Ridgecrest $M7.1$ and $M6.5$ ruptures, respectively (modified from [*Chen et al., 2020*]); Lower panels show displacement deviations, colored as to highlight the normal component (perpendicular to the main shock rupture) as of 1 April 2018 (b), and 15 May 2018 (c). The star shows the main shock epicenter.

full geomechanical simulation to infer stress distribution. Concerning the 2019 Ridgecrest earthquake, the most clear localization anomaly was identified approximately 60–70 km to North-West off its epicenter.

Within the proposed framework combining cascade-up and progressive localization concepts all-together with the full stress and strain modelling, we have obtained SD distribution timeseries, which have enabled tracking a specific SD localization pattern prior to the earthquake, complemented by directional analysis of local weakening-associated displacement perturbations.

It was found that about a year before the event, the large-scale earthquake preparation processes reached their maximum extent, spreading across the entire San Andreas fault area and manifesting as numerous SD anomalies with chaotic displacement orientation. Along with such background regional-scale activation, some local SD anomalies, only typical for the epicentral zone (EZ) of the future Ridgecrest earthquake, had their final development.

At the same time, about 3 years prior to the event, local SD anomalies appear, which can be considered as early manifestations of short-term precursors. An alternation of peak SD levels and quiescence intervals, with cycle duration of several months, was revealed from the simulated SS data. This behavior can be explained in terms of the well-known avalanche unstable fracturing model and dilatancy-diffusion model. A possible mechanism for such effects is fracturing causing the decrease in pore pressure, which leads to rock hardening.

Under continuous influence of background tectonic forces, the maximum SD zones tend to move into the surrounding region until the rocks in the EZ return to an unstable state, which resembles swinging. Such swinging, as well as the alternation of SD levels over time, with peaks and quiet periods, altogether called excursions, can significantly limit the capabilities of forecasting, causing so-called false alarms, when despite the strain reaches (sub)critical levels, the earthquake still does not occur and the stress state returns back to another quiet.

In this regard, it becomes necessary to involve additional parameters in the analysis that can eliminate such ambiguity. One of those parameters, possibly, is the displacement vector direction. The results obtained show that even with the highest SD values observed 3 and 2 years before the event, the earthquake does not occur if the displacement directions don't coincide with the future rupture orientation. And only a year prior to the event, those directions stabilize, and the structure of the Ridgecrest strike-slip fault begins to form. The very formation of the focus occurs as a preparation for the "bridge" destruction with the sequential appearance of SD anomalies at its ends with cyclic interval of several months. The obtained result is in agreement with theoretical and laboratory studies with the only difference that the latter didn't consider the destruction precursors prior to the shock. Following the "swing" terminology when describing the preparation of the "bridge" destruction, we can conclude that the earthquake occurred after the fifth swing and only when displacement direction got stabilized and consistent with the future rupture. Perhaps the appearance of a local extension zone throughout the entire future rupture 5 days before the event also played a role.

And finally, through a separate analysis of the orthogonal components of the simulated displacement field, with a primary role of the normal one, we identified and discriminated and SD region coinciding with the location of the $M6.5$ foreshock rupture.

5. Conclusions

The results obtained help to better understand the stress-strain dynamics prior to 2019 Ridgecrest earthquake, the most recent major seismic event in Southern California, suggesting that the proposed monitoring technique might contribute to the short-term forecasting methods. As a key parameter, we have primarily focused the analysis on shear strain intensity dynamics (SD), which determines the structure of the Ridgecrest rupture. The advantages of the modelling-based monitoring are related to the fact that the full tensor stress-strain state and kinematic quantities, including the displacement field directions, are computed at different depths within the subsurface and allow for pattern recognition and tracking, while at the Earth's surface both SD and displacement levels are significantly lower or nearly zero. Cyclic patterns (swing-like periodic migration) identified in the simulated shear strain anomalies, with estimation of their

spatial and temporal characteristics, along with tracked variations in local displacement orientation provide evidence for progressive predominant orientation of crustal-deep strains fairly close to future rupturing direction during the last stages of earthquake preparation.

Acknowledgments. We'd like to acknowledge the helpful discussions and advice from our colleagues at Schmidt Institute of Physics of the Earth RAS. The study was supported by Institute for Scientific Research of Aerospace Monitoring "AEROCOSMOS" (project No. 122011800095-3).

References

Akopian, S. Ts., V. G. Bondur, E. A. Rogozhin (2017), Technology for monitoring and forecasting strong earthquakes in Russia with the use of the seismic entropy method, *Izvestiya, Physics of the Solid Earth*, *53,* No. 1, 32–51, **Crossref**

Argus, D. F., R. G. Gordon (1991), No-net-rotation model of current plate velocities incorporating plate motion model NUVEL-1, *Geophys. Res. Lett.*, *18,* 2039–2042.

Ben-Zion, Y., I. Zaliapin (2019), Spatial variations of rock damage production by earthquakes in southern California, *Earth Planet. Sci. Lett.*, *512,* 184–193.

Ben-Zion, Y., I. Zaliapin (2020), Localization and coalescence of seismicity before large earthquakes, *Geophys. J. Int.*, *223,* 561–583.

Bondur, V. G., A. T. Zverev (2005), A method of earthquake forecast based on the lineament analysis of satellite images, *Doklady Earth Sciences*, *402,* No. 4, 561–567.

Bondur, V. G., I. A. Garagash, et al. (2007), Geomechanical models and ionospheric variations related to strongest earthquakes and weak influence of atmospheric pressure gradients, *Doklady Earth Sciences*, *414,* No. 4, 666–669, **Crossref**

Bondur, V. G., I. A. Garagash, et al. (2010), Connection between variations of the stress–strain state of the Earths crust and seismic activity: the example of Southern California, *Doklady Earth Sciences*, *430,* Part 1, 147–150, **Crossref**

Bondur, V. G., I. A. Garagash, et al. (2016), The evolution of the stress state in Southern California based on the geomechanical model and current seismicity, *Izvestiya. Physics of the Solid Earth*, *52,* No. 1, 117–128, **Crossref**

Bondur, V. G., M. B. Gokhberg, et al. (2020a), Some challenges of short-term earthquake forecasting and possible solutions, *Doklady Earth Sciences*, *495,* No. 2, 910–913, **Crossref**

Bondur, V. G., M. B. Gokhberg, et al. (2020b), Revealing short-term precursors of the strong $M > 7$

earthquakes in Southern California from the simulated stress-strain state patterns exploiting geomechanical model and seismic catalog data, *Frontiers in Earth Science*, *8,* 571,700, **Crossref**

Bondur, V. G., M. B. Gokhberg, et al. (2021), Early manifestations of short-term precursors in stress-strain state dynamics of Southern California, *Izvestiya. Physics of the Solid Earth*, *4,* 1–13, **Crossref**

Bondur, V. G., M. N. Tsidilina, et al. (2018), Systematization of Ionospheric, Geodynamic, and Thermal Precursors of Strong ($M \geq 6$) Earthquakes Detected from Space, *Izvestiya, Atmospheric and Oceanic Physics*, *54,* No. 9, 1172–1185, **Crossref**

Chen, K., J.-P. Avouac, et al. (2020), Cascading and pulse-like ruptures during the 2019 Ridgecrest earthquakes in the Eastern California Shear Zone, *Nature Comms.*, *11,* 22, **Crossref**

Clayton, R. W., T. Heaton, et al. (2015), Community Seismic Network: a dense array to sense earthquake strong motions, *Seismological Research Letters*, *86,* 1354–1363, **Crossref**

Dieterich, J. H. (1992), Earthquake nucleation on faults with rate-and state-dependent strength, *Tectonophysics*, *211,* 115–134, **Crossref**

Garagash, I. A. (2000), Application of azimuthal variations of seismic waves velocity for the seismic hazard monitoring in Kamchatka, *Problems in seismicity of the Far East* p. 164–175, KOMSP GS RAS, Petropavlovsk-Kamchatsky.

Hutton, L. K., J. Woessner, E. Hauksson (2010), Seventy-Seven Years (1932–2009) of Earthquake Monitoring in Southern California, *Bull. Seismol. Soc. Am.*, *100,* No. 2, 423–446, **Crossref**

Itasca Consulting Group (2006), *Inc. FLAC3D – Fast Lagrangian Analysis of Continua in 3 Dimensions, Ver. 3.1, User's Manual*, Itasca, Minneapolis.

Kato, A., Y. Ben-Zion (2021), The generation of large earthquakes, *Nat. Rev. Earth Environ.*, *2,* 26–39, **Crossref**

Main, I. G., A. F. Bell, et al. (2012), The dilatancy–diffusion hypothesis and earthquake predictability, *Geological Society, London, Special Publications*, *367,* 215–230, **Crossref**

Mogi, K. (1985), *Earthquake Prediction*, Academic Press, Tokyo.

Molchan, G., V. Keilis-Borok (2008), Seismology Earthquake prediction: probabilistic aspect, *Geophys. J. Int.*, *173,* 1012–1017.

Myachkin, V. A., B. V. Kostrov, et al. (1975), Principles of source physics and earthquakes precursors, *Physics of Earthquake Focus* p. 6–29, Nauka, Moscow.

Parsons, T. (2006), Tectonic stressing in California modeled from GPS observations, *J. Geophys. Res.*, *111,* B03407, **Crossref**

Sobolev, G. A. (1993), *Fundamentals of Earthquake Forecast*, 313 pp. Nauka, Moscow.

Sobolev, G. A. (2019), Avalanche Unstable Fracturing Formation Model, *Izv., Phys. Solid Earth*, *55,* 138–151, **Crossref**

Sobolev, G. A., A. V. Ponomarev (2003), *Physics of Earthquakes and Precursors*, 270 pp. Nauka, Moscow.

Wallace, R. E., Ed. (1990), The San Andreas fault system, California, *U.S. Geological Survey Professional Paper*, *1515,* 283. (https://pubs.usgs.gov/pp/1990/1515/pp1515.pdf)

Yoon, C. E., N. Yoshimitsu, et al. (2019), Foreshocks and mainshock nucleation of the 1999 Mw7.1 Hector Mine, California, earthquake, *J. Geophys. Res. Solid Earth*, *124,* 1569–1582, **Crossref**

Corresponding author:

Dmitry A. Alekseev, Schmidt Institute of Physics of the Earth RAS, B. Gruzinskaya str., 10, build. 1, 123242 Moscow, Russia. (alexeevgeo@gmail.com)